Journal of Materials Chemistry A

ROYAL SOCIETY OF CHEMISTRY

PAPER

View Article Online
View Journal | View Issue

Cite this: J. Mater. Chem. A, 2025, 13, 31292

Synthesis, assembly, and electrochemical performance of ultrasmall Sb_2S_3 nanoparticles

Zachery R. Wylie,[a] Guesang K. Lee,[a] Soohyung Lee,[a] Abdul Moeez,[b] Guodong Ren,[c] Juan-Carlos Idrobo,[cd] Peter J. Pauzauskie,[c] Lilo D. Pozzo*[ab] and Vincent C. Holmberg[ab]

Received 24th May 2025
Accepted 11th August 2025

DOI: 10.1039/d5ta04184h

rsc.li/materials-a

A synthetic pathway to ultrasmall antimony(III) sulfide nanoparticles is demonstrated using scalable, room-temperature, and open-atmosphere procedures that only requires commonly available precursors. The synthesis is accompanied by the immediate self-assembly of nanoparticles, which is characterized using small angle X-ray scattering (SAXS). During the synthesis, particles assemble into stable mesophases that exhibit unusual 'rod-like' hexagonal packing, which is unexpected from discrete nanoparticles lacking crystallographic registry. It is demonstrated that the resulting superstructures are effectively manipulated by compositional changes to the ligand and solvent environment. Ligands, which are chemically related short-chain alkyl molecules, direct the assembly of Sb_2S_3 nanoparticles and also influence the performance of negative electrodes in Li^+ and Na^+ battery systems. Integration of Sb_2S_3 materials in batteries yields impressive capacity, charge/discharge rates, and cyclability.

1. Introduction

Antimony(III) sulfide (Sb_2S_3) is an environmentally friendly material of interest for thermoelectric,[1,2] photovoltaic,[3–5] and electrochemical applications.[6–8] It is found naturally in a layered orthorhombic phase (*Pmna*), where it has been known since antiquity as stibnite,[9] but under certain conditions an amorphous phase is also accessible.[10,11] As is the case with many metal chalcogenide systems, Sb_2S_3 benefits from nanostructuring, particularly in colloidal synthesis routes, to improve and tailor its properties.[8,12] Colloidal nanoparticles have larger specific surface areas, tunable sizes, morphology dependent properties, and are solution processable.[13] Because of this, expanding the library of colloidal synthesis routes towards useful morphologies of Sb_2S_3 has continued to be impactful to a diverse range of technologies.[14–17] Sb_2S_3 has been synthesized colloidally using a variety of methods producing several structures and forms. Since the most thermodynamically stable product is crystalline orthorhombic, micro and nanoparticles commonly manifest as wires,[18] bundled rods,[19] and even 'flowers'.[20] In contrast, the amorphous phase is spherical when synthesized using solvothermal bottom-up strategies.[8,14,21,22] Sizes for particles, crystalline and amorphous, range from ~20 nm to many hundreds of micrometers, but some cases of smaller nanoparticles (<10 nm) also exist in literature.[16,23]

The synthesis of ultrasmall colloidal particles, defined as particles smaller than ~5 nm in diameter, can often require highly involved procedures.[24] At these sizes, unstable atomic arrangements become easier to access due to the increase in surface area relative to volume.[25] Magic-sized clusters, having specific numbers of atoms producing stable structures, are a prototypical example exhibiting unique optical characteristics and self-assembly.[26] Nanoparticle assembly into stable structures is affected by the shape and morphology of the particles,[27] by the use of templates (*e.g.* patterned surfaces or self-assembling polymers),[28,29] by surface bound ligands,[30] by external fields,[31] and by registered crystallographic directions. With respect to crystallographic registry, this can be mediated either through the attachment of specific facets,[32] or by the facet-specific capping of ligands which can influence alignment of nanocrystals during packing.[33] Because of this, the nanoparticle structure and morphology are strong predictors for highly ordered self-assembly in the absence of a template or external field. For example, large aspect ratio nanostructures pack into hexagonal arrays,[34,35] and monodisperse spheres typically experience close packing into face-centered cubic or hexagonal close-packed lattices.[36,37]

Sb_2S_3 has also received significant attention as a battery material for both Li^+ and Na^+ ion systems. It is able to undergo both alloying and conversion reactions with Li^+/Na^+ at the negative electrode giving it a theoretical capacity of 946 mAh g^{-1}

[a]Department of Chemical Engineering, University of Washington, Seattle, WA 98195, USA. E-mail: dpozzo@uw.edu

[b]Molecular Engineering and Sciences Institute, University of Washington, Seattle, WA 98195, USA

[c]Department of Materials Science and Engineering, University of Washington, Seattle, WA 98195, USA

[d]Physical and Computational Sciences Directorate, Pacific Northwest National Laboratory, Richland, WA, 99354, USA

compared to graphite's 372 mAh g^{-1}.[6] Its rate capabilities are also impressive, with certain Sb_2S_3 electrodes able to withstand cycling at rates up to 20C (~3 min charge/discharge).[8] As such, Sb_2S_3 stands to be impactful in electrifying machines that draw large currents or benefit from faster charging than what current battery technologies can support.[6] One challenge with Sb_2S_3 is that the highest performing batteries are exclusively made using bottom-up processes to produce a nanoscale active material,[8,38,39] which complicates production at relevant scales and low cost. The commercialization of Sb_2S_3 as an electrode material would greatly benefit from simplified synthetic procedures that lower the cost of preparation.

To this end, we synthesize ultrasmall antimony(III) sulfide (Sb_2S_3) nanoparticles (<4 nm) using a simple one-step, room temperature, procedure in open air. Small angle X-ray scattering (SAXS) measurements demonstrate that these nanoparticles assemble into unusual long-range hexagonal 'rod-like' packings, which we attribute to a non-uniform coating over the surface of the particles. The spacing and structure of the arrangement can be fine-tuned by changing the composition and length of the alkylamine ligands and solvent. The Sb_2S_3 nanoparticles also exhibit impressive electrochemical performance when prepared as a negative Li^+ and Na^+ ion battery electrodes. Different ligands influence the packing arrangement, and electrochemical data shows significant differences between these samples even after a ligand exchange. Thus, the identity of the ligand used in the synthesis of Sb_2S_3 nanoparticles has significant impacts for assembly as well as electrochemical performance.

2. Experimental

2.1. Materials

All chemicals were used as received unless specified otherwise. Antimony(III) acetate ($Sb(OAc)_3$, 99.99% trace metals basis), ammonium sulfide solution ($(NH_4)_2S$, 20 wt% in water), ammonium sulfide solution ($(NH_4)_2S$, 40–48 wt% in water), octylamine (OcAm, 99%), dodecylamine (DoAm, 98%), oleylamine (OAm, >98% (primary amine)), trioctylphosphine (TOP, 97%), trioctylphosphine oxide (TOPO, 99% ReagentPlus), hydrazine monohydrate (N_2H_2, 64–65%), were purchased from Sigma-Aldrich. Toluene, ethanol, and other common solvents were purchased from Fischer Scientific and used as received.

Battery grade 1.0 M $LiPF_6$ in EC/DMC = 50/50 (v/v), propylene carbonate (99.7%), sodium metal (>99.99%, dry cubes, ACS Specification), sodium carboxymethyl cellulose (CMC) ($M_w \sim 90\,000$) were purchased from Sigma Aldrich. Sodium perchlorate (≥98%) was purchased from Fisher Scientific. Fluoroethylene carbonate (≥98%) was purchased from TCI America. Carbon black (Vulcan XC72R) was purchased from Cabot Corporation and stored in a vacuum oven at 80 °C. CR2032 coin cell cases (SS316 Option), CR20XX stainless steel spacer (15.5 mm dia. × 0.4 mm), stainless steel wave spring, copper foil (>99.99%, 9 μm thickness), 600 μm thick lithium chip (Battery R&D grade) were purchased from MTI Corporation. Celgard separator (Celgard 2400, 25 μm microporous monolayer polypropylene membrane, Celgard Inc. USA), glass microfiber separator (GF/D, cat no. 1823-257, Whatman).

2.2. Synthesis of ultrasmall antimony(III) sulfide nanoparticles

The synthesis of ultrasmall Sb_2S_3 was adapted from a procedure used by Zhang *et al.* for different chalcogens.[40] First, a 0.1 mM $Sb(OAc)_3$ solution was prepared in a 1 : 1 ratio by weight of toluene and alkylamine ligand (octylamine, dodecylamine, or oleylamine) by sonicating for 15 minutes. The total mass of solution was 5 g. After sonicating, a stir bar was added, and the supersaturated milky white solution of $Sb(OAc)_3$ was stirred vigorously. While stirring, 0.5 mL of ammonium sulfide solution (20 wt%, aqueous) was added quickly, making the total sulfur concentration 0.245 mM. The reaction immediately turned a reddish brown, remained turbid, and was stirred for ~1 min to ensure a completed reaction. The solution was then transferred directly to a quartz capillary for SAXS characterization of the as-synthesized nanoparticles and their assembly. This synthesis procedure deviates from the methodology of Zhang *et al.* in key ways that render the process more amenable for commercial scales. First, using a lower concentration (20 wt%) of aqueous ammonium sulfide allows for the direct injection of the sulfur reagent into the antimony acetate solution. We find that, for this material system, additional drying and preparation of the ammonium sulfide precursor into an alkylamine solution is unnecessary. Secondly, the preparation of the cation solution is also performed at room temperature, whereas Zhang *et al.* specify much more elevated temperatures to ensure complete dissolution of the metal salts, sometimes under nitrogen to prevent oxidation. Conversely, with antimony acetate, we observed an opaque white solution indicating incomplete dissolution. Under these reaction conditions, antimony acetate is prone to oxidize but its sulfurization is still able to proceed (Fig. S6). The ability to conduct the entire process in open air, at room temperature, and without drying or intensive preparation of precursors is attractive for commercial production.

2.3. Dry synthesis of antimony(III) sulfide nanoparticles

More closely following Zhang *et al.*,[40] a dried ammonium sulfide solution in octylamine was prepared in open air to be used as the source of sulfur for the room temperature synthesis of ultrasmall Sb_2S_3 nanoparticles. First, 0.8 mL of 40–48 wt% aqueous ammonium sulfide was added to 10 mL of octylamine and stirred. After 15 minutes, activated 3.4 Å molecular sieves were added and allowed to stir for an additional 15 minutes. A 2 mL aliquot of this solution was then injected into the 0.1 mM $Sb(OAc)_3$ solution which was prepared as previously described with a mixture of 50 wt% octylamine and 50 wt% toluene using 15 min of sonication. Molecular sieves were activated *via* heating at 110 °C under vacuum for approximately 48 hours.

2.4. Scanning transmission electron microscopy

Scanning transmission electron microscopy (STEM) samples were prepared by the drop casting of diluted nanoparticles onto

carbon film, 200 mesh nickel grids (Electron Microscopy Sciences; Hatfield, PA). STEM imaging was performed using an aberration-corrected Nion UltraSTEM 100 operated at 60 kV with a convergence semi-angle of 32 mrad. High-angle annular dark field (HAADF) images were acquired using an annular dark-field detector with inner and outer collection semi-angles of 80 and 200 mrad, respectively.

2.5. Fourier transformed infrared spectroscopy

Attenuated total reflectance Fourier transformed infrared spectroscopy (FTIR) was performed using a Thermo Fisher Scientific Nicolet IS50R equipped with a diamond window at a resolution of 2 cm^{-1}. Solid nanoparticle samples were dried overnight under vacuum prior to measurement.

2.6. X-ray scattering sample preparation and measurement

Immediately after the previously described synthesis of Sb_2S_3 nanoparticles, the nanoparticle reaction solution was transferred into a quartz capillary. Thin walled (10 μm) 1.5 mm diameter quartz capillaries were purchased from Hampton Research (Aliso Viejo, CA) and were sealed with two part 5 minute epoxy from Devcon (Illinois Tool Works; Danvers, MA). Small angle X-ray scattering (SAXS) was performed on a Xenocs Xeuss 3.0 (Grenoble, France) powered by microfocus GeniX 3D X-ray generator for Cu Kα (0.15406 nm wavelength) and a Dectris EIGER 2 1M X-ray detector. The measurements were made at detector distances of 1.80 m, 0.90 m, 0.37 m and 0.05 m. The 2D images recorded were reduced and merged using XSACT 2.10 from Xenocs (Grenoble, France). Peak positions were determined using Origin 2016 from OriginLab (Northampton, MA).

X-ray diffraction data was acquired using a Bruker D8 Discover Microfocus powder X-ray diffractometer equipped with a Pilatus 100K large-area 2D detector with X-ray source (Cu tube Kα radiation 1.54184 Å) operating at 100 mA and 50 kV. Samples were drop-cast onto silicon wafer under ambient conditions.

2.7. Preparation of Sb_2S_3 electrode material

To prepare an electrode from ultrasmall Sb_2S_3 nanoparticles, the nanoparticles first had to be washed, followed by a ligand stripping procedure. After the reaction, the turbid solution of particles was transferred to a falcon tube with 5 mL of ethanol and centrifuged at 5000 rpm (2907 × *g*) for 3 minutes before resuspending in toluene. This process was repeated 3 times. To strip the ligands, the NPs were first dispersed in acetonitrile through vortexing and sonication before transferring to a dram vial and stirring vigorously with a stir bar. The acetonitrile is a poor solvent for the alkylamine coordinated NPs, so the solution appeared more aggregated. An autoinjector was used to dispense 2 mL of hydrazine monohydrate (N_2H_2, 64–65%) into the solution at a rate of 0.025 mL min^{-1} over 2 hours. The final volume of the resulting solution was approximately 25 mL and 1 M of hydrazine. As the ligands were stripped by the hydrazine, the NPs sedimented and deposited onto the glass of the dram vial over the course of the process. Once all the NPs had sedimented, the acetonitrile supernatant was discarded, and the deposited particles were dispersed back into a small amount of acetonitrile and nanopure water (18.2 MΩ cm^{-1}) in a 1 to 1 ratio using sonication and dried using a rotovap. Qualitatively, the ligand exchange could be deemed successful as polar solvents suspended the nanoparticles more thoroughly than nonpolar solvents after the exchange.

Once dry, the NPs were mixed using an agate mortar and pestle with conductive carbon (Super P) and sodium carboxymethyl cellulose (Na CMC) dissolved in water at a concentration of 33 mg mL^{-1} in a ratio of 64 : 21 : 15. This ratio was used following the battery preparation of Kravchyk *et al.* using other antimony sulfide nanoparticles.[8] Once the slurry was homogenous, a 12.7 μm (0.5 mil) electrode was coated on copper foil using a stainless-steel doctor blade. The printed electrodes are dried on a heating plate at 80 °C then stored in a vacuum oven set to 90 °C for >24 h until needed. 15 mm electrode punch-outs resulted in an areal electrode loading that ranges from 0.5–0.8 mg cm^{-2}. Similar loadings were used for fair comparison between the samples.

2.8. Electrochemical characterization

All electrochemical characterization was done in a 2032 coin cell configuration. Coin cells were assembled in an argon-filled glovebox (O_2 < 1 ppm, H_2O < 1 ppm). For Li-ion, one layer of glass fiber and one layer of polypropylene membrane were used as the separator with 150 μL of 1 M $LiPF_6$ in EC : DMC (1 : 1 v/v) with 3 wt% FEC. For Na-ion batteries, one layer of glass fiber separator was used with 100 μL of 1 M $NaClO_4$ in propylene carbonate (PC) with 3 wt% FEC. Li and Na metals were used as counter electrodes. Electrochemical measurements were performed using a constant current mode for both, charge and discharge between 0.01–2.0 V on a MACCOR (Tulsa, OK) 64 channel Battery Tester.

3. Results

3.1. Synthesis of ultrasmall Sb_2S_3 nanoparticles

The room temperature synthesis of ultrasmall Sb_2S_3 nanoparticles is achieved by dissolving antimony(III) acetate ($Sb(OAc)_3$) in toluene and an alkylamine followed by the fast injection of a 20 wt% aqueous solution of ammonium sulfide, $(NH_4)_2S$, at room temperature under vigorous stirring. The opaque white $Sb(OAc)_3$ solution turns a turbid reddish brown immediately as nanoparticles form (Fig. 1A). The solution is vigorously stirred with a stir bar for 1 minute to ensure a complete reaction. The formation of a turbid solution and a low-density precipitate, which sediments within a few hours, suggests the presence of large structures within the dispersion. Since the reaction benefits from vigorous stirring, we found octylamine to be most suitable for synthesis as higher melting point alkylamines tend to form a gel following the reaction. To characterize these materials, SAXS was used to probe the 'as-synthesized' matrix. Using SAXS, the presence of highly ordered structures within the nanoparticle dispersion was identified (Fig. 1C). The turbid solution was found to contain long (>300 nm) assemblies in a 'rod-like' hexagonal packing, which is easily distinguishable from typical cubic closed-packed

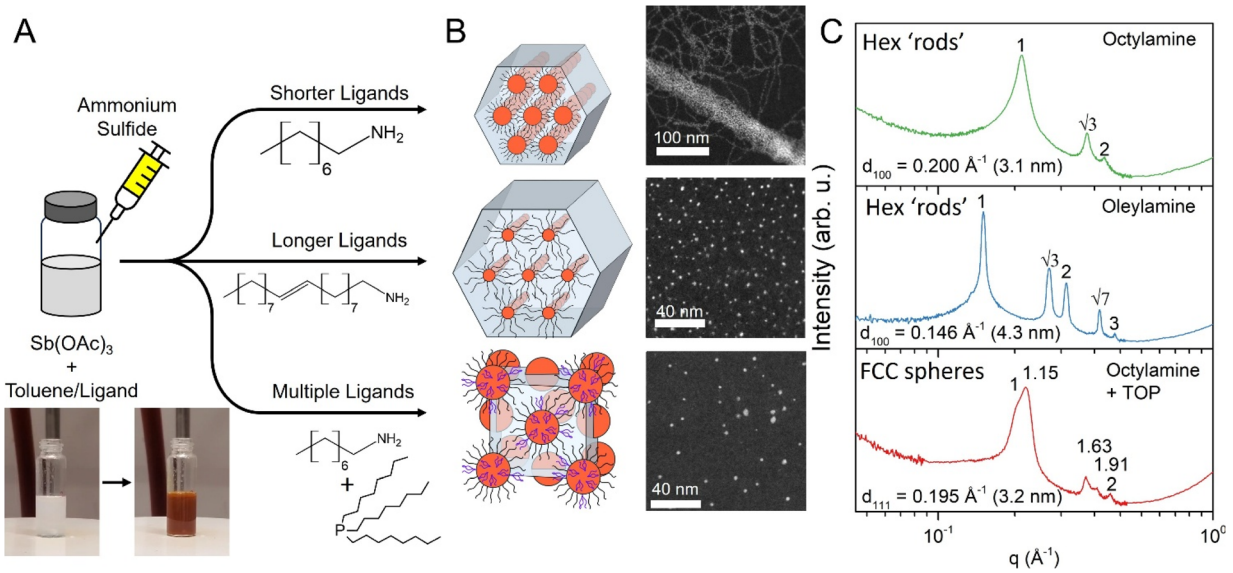

Fig. 1 Diagram depicting (A) the room temperature, open air, reaction between antimony acetate ($Sb(OAc)_3$) and 20 wt% aqueous ammonium sulfide using ligands of different lengths (octylamine and oleylamine) and chemistries (trioctylphosphine) to produce (B) ultrasmall (~3 nm) Sb_2S_3 nanoparticles identified with scanning transmission electron microscopy (STEM) in high-angle annular dark field (HAADF) imaging mode. (C) Small angle X-ray scattering measurements of the as-synthesized reaction matrix reveals the particles order into a mesophase with tunable arrangements and spacings in the as-synthesized matrix.

structures.[41,42] The sharpness of peaks, and their magnitude, suggests a strongly scattering medium with a high degree of order. This result, in conjunction with the high turbidity and formation of precipitates, suggests that a mesophase is produced after the reaction.[43]

The structure of the mesophase of assembled nanoparticles is further controllable by changing the length and functional group of the ligands. Fig. 1B shows this graphically. Shorter alkylamines, like octylamine, reduce the center-to-center spacing (d_{100}) of the 'rods', while longer ligands, such as oleylamine, increase the spacing while maintaining the same hexagonal structure (Fig. 1C). The spacing in the [100] direction, which is attributed to the position of the first scattering peak, when using a 50 wt% solution of octylamine in toluene was 0.200 $Å^{-1}$ (3.1 nm), while an equal weight percent of oleylamine gave spacings of 0.146 $Å^{-1}$ (4.3 nm). Given that the spacings are only a few nanometers larger than the extended lengths of the alkylamines, octylamine has an approximate length of 1.0 nm and oleylamine is approximately 2.04 nm long when fully extended,[44,45] the particles are ultrasmall in all cases (1–4 nm) and coordinated by ligands. These particle sizes were confirmed using HAADF-STEM (Fig. S1–S4). The same hexagonal structure is not maintained, however, when 10 wt% of another ligand, trioctylphosphine (TOP), is added in conjunction with octylamine. Instead, the structure becomes a face-centered cubic spherical arrangement with a d_{111} spacing of 0.195 $Å^{-1}$ (3.2 nm). The 'rod-like' hexagonal organization that is observed for all pure alkylamine ligands is unusual for spherical particles since there is no obvious driver for assembly into linear arrays.[29,46,47]

From high-resolution aberration-corrected scanning transmission electron microscopy (STEM) in high-angle annular dark field (HAADF) imaging mode, it is determined that the Sb_2S_3 primary particles are ultrasmall, discrete, and roughly spherical. However, depending on the ligand, the particles can also form fibrous structures (Fig. S1). These fibers are like those previously reported by Nevers *et al.* in syntheses of CdS magic-sized clusters.[43] These researchers reported a similar hexagonal structure of ultrasmall nanoparticles, and suggest that formation of a mesophase halts the growth of the particles by sequestering nucleation sites away from monomers in the reaction solution. The reaction solution being supersaturated is also thought to be critical in making nucleation more prevalent than growth for this and other ultrasmall systems.[48,49] Still, the exact cause for the stability during formation of particles in this size regime is debated.[26]

The synthesis reported in this work produces similar particles when using other alkylamines, namely dodecylamine and oleylamine. However, a fibrous morphology was not observed in HAADF-STEM (Fig. S3 and S4) for these samples. Primary particles were not found to be crystalline, and lattice fringes were not distinguishable in HAADF-STEM in any sample. While HAADF-STEM can provide information on the morphology of the primary particles, SAXS is a preferable technique for characterizing assembly since it can probe the structures in the dispersed state without the need for solvent removal. In contrast, morphologies are anticipated to be altered by preparation of samples for imaging due to washing steps required to remove excess ligands and the requisite evaporation of the solvent. This is commonly seen in other nanoparticle systems where the solvent is a critical component to the assembly, and drying disrupts the structure.[43,50–52]

In this system, the concentration of reagents contributed greatly to the presence of the 'rod-like' mesophase, since lower concentrations of $Sb(OAc)_3$ led to no assembly in solution

(Fig. S5B). When $Sb(OAc)_3$ was in excess (at high concentrations of Sb^{3+} or low concentrations of S^{2-}) a cubic antimony(III) oxide phase (senarmontite, PDF #98-002-0076) was observed in the wide-angle X-ray scattering (WAXS) range. Since all steps in the synthesis were performed in open air, oxide formation is expected when excess Sb^{3+} is left unreacted. We also note that, in a typical synthesis (Fig. S5A), there is a single peak in the WAXS region at 2.21 $Å^{-1}$ (0.28 nm). While a single peak is insufficient to assign it to be the bulk orthorhombic phase of Sb_2S_3 (stibnite, PDF# 98-000-0411), it is within the approximate range of lattice spacings of layered bulk stibnite.[53] This indicates that while particles may be too small to be accurately called 'amorphous', they do not show evidence of strong crystallinity. Regardless of the choice of ligand, no variations are observed in the position of this WAXS feature between Sb_2S_3 samples. These results are corroborated using X-ray diffraction which can observe higher q values and angles in 2θ (Fig. S6).

3.2. Structure of self-assembled nanoparticle mesophases

In addition to synthesizing ultrasmall Sb_2S_3 nanoparticles, the spacings in the hexagonal 'rod-like' packing were shown to be controllable by changing the length and concentration of alkylamine ligands. Three different ligands were evaluated for variations in length: octylamine (8 carbons), dodecylamine (12 carbons), and oleylamine (18 carbons) (Fig. 2A). The shortest ligand, octylamine, produced the closest packing with a center-to-center spacing of 3.1 nm. Dodecylamine and oleylamine are substantially longer ligands and produce spacings of 3.7 and 4.3 nm respectively. All alkylamine samples shared the same signature Bragg spacings of hexagonal close-packed 'rods' with peaks at scattering vectors of q, $\sqrt{3}q$, $2q$, and $\sqrt{7}q$ corresponding to d_{hk0} lattice spacings d_{100}, d_{110}, d_{200}, and d_{210} respectively.[41] The peak position in q-space (q) is converted to real-space (d) by the relationship $d = 2\pi/q$ where q is in units of inverse length.[54] The longest ligands produced the narrowest peaks, which is indicative of a uniform structure containing large domains in the scattering medium.[55]

The lattice spacings were also tuned by adjusting the concentration of the alkylamine ligand in the solution. In these syntheses, the ligand was replaced with the same mass of toluene over the workable range. For octylamine (Fig. 2B), the syntheses ranged from no added ligand (0 wt%), to pure octylamine (90 wt% of the total mass including precursors). When no ligand was added, the Sb_2S_3 particles deposited immediately onto the walls of the vial as it was unstable in solution without a ligand. Lower concentrations of octylamine gave larger

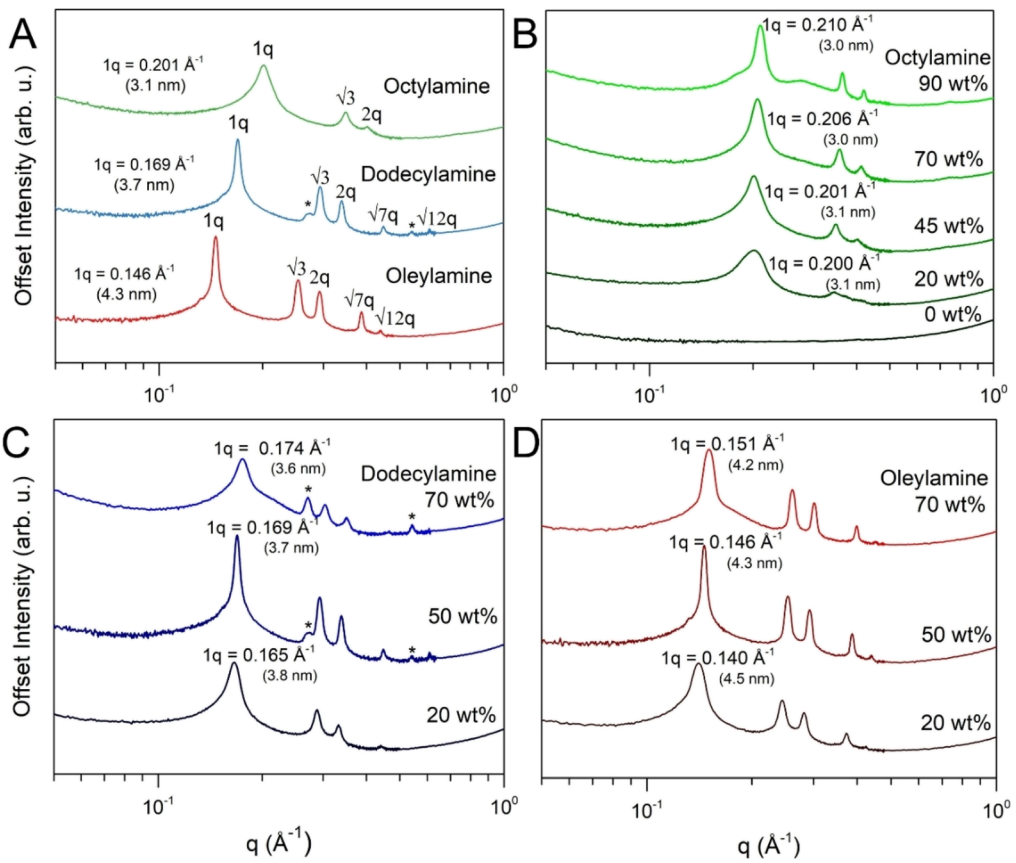

Fig. 2 SAXS profiles for Sb_2S_3 syntheses using (A) 50 wt% solutions of three alkylamines with a range of chain lengths. Syntheses were performed with these three alkylamines, (B) octylamine, (C) dodecylamine, and (D) oleylamine with variable concentrations ranging from 20 wt% to 70 wt% or more. In dodecylamine samples, lamellae formed when the ligand was not fully dissolved. These follow a peak spacings of 1q (at 0.271 $Å^{-1}$) and 2q. Both are marked with an asterisk. All axes are in log scale.

particle spacings and broader peaks while higher concentrations produced tighter spacings and narrower peaks.

Nanoparticles prepared from longer ligands displayed similar trends. The spacing for dodecylamine (Fig. 2C) and oleylamine (Fig. 2D) assemblies change over a 0.2 nm and 0.3 nm range respectively as the ligand concentration is altered. The variation was proportional to the total number of carbons in the alkyl chain. While octylamine produced sharper features on increasing concentration, dodecylamine and oleylamine showed the sharpest features at ~50 wt% ligand before broadening again above 70 wt%. An added complication, which was unique to dodecylamine, was that high concentrations of the ligand precipitated to form crystalline lamellar phases. This produced smaller peaks in the SAXS data that increased in intensity with increasing concentration of dodecylamine at ratios of $1q$ (0.271 $Å^{-1}$, 2.3 nm) and $2q$ (marked with an asterisk in Fig. 3C).[56] No lamellae were observed below 20 wt%, and no peak shift was observed between 50 and 70 wt% ligand.

Since this synthesis procedure involved the addition of an aqueous reagent (~0.5 mL of aqueous 20 wt% $(NH_4)_2S$) to a nonpolar organic solution (~5 mL toluene and alkylamine), the potential influence of water on the structure of the assembly was determined. SAXS data was collected on samples synthesized with octylamine at different concentrations, while also preparing corresponding backgrounds by centrifuging each sample at 10 000 rpm ($5814 \times g$) and collecting the supernatant, absent of particles, for measurement (Fig. 3A). SAXS showed the hexagonal 'rod-like' structure for as-synthesized samples, while the corresponding background only shows a broad feature that shifts to higher angles (0.21 $Å^{-1}$ to 0.28 $Å^{-1}$) as the concentration of octylamine increases. This feature may result from the spacing between reverse micelles of solvated water molecules. To demonstrate that this feature is independent of the assembly of nanoparticles, we followed a procedure by Zhang *et al.* for transferring and drying aqueous ammonium sulfide into a liquid alkylamine using 3 Å molecular sieves.[40] Details for the procedure can be found in the methods section. Both samples in Fig. 3B were prepared with 1 : 1 octylamine to toluene by weight. Two samples were prepared following this procedure: one that was dried with molecular sieves and a control that had no molecular sieves. SAXS was collected for both along with a corresponding background prepared by centrifugation and separation of the supernatant (Fig. 3B). In both the dried sample with sieves and the control without sieves, the 'rod-like' hexagonal structure is still maintained while the intensity of the broad feature belonging to solvated water decreases. Since the same hexagonal mesophase is obtained using both 'dry' (Fig. 3B) and 'wet' methods (Fig. 3A), assembly involves primarily Sb_2S_3 particles and ligands. Thus, it is independent from water introduced into the system.

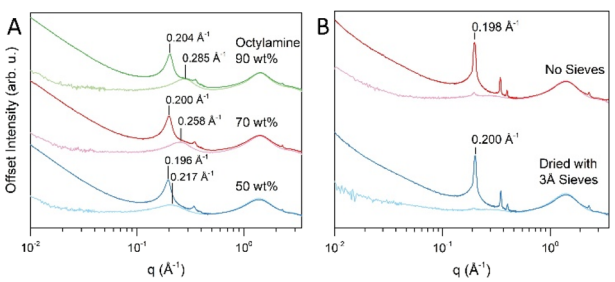

Fig. 3 SAXS of control samples where (A) the synthesis of Sb_2S_3 nanoparticles using 90, 70, and 50 wt% of octylamine (dark lines). The nanoparticles assemble into hexagonal 'rod-like' arrangement and the d_{100} peak shifts with higher concentrations of octylamine. Background scattering of the solvents (lighter lines) were collected on the centrifuged supernatants of the same samples. (B) SAXS of control syntheses comparing drying of the aqueous ammonium sulfide into pure octylamine. One (blue) was dried with molecular sieves and the other (red) followed the same procedure of transferring the $(NH_4)_2S$ (aq.) to octylamine, but no sieves were added. Both axes are in log scale.

3.3. Altering nanoparticle self-assembly with multiple ligands

Ultrasmall Sb_2S_3 particles, which are expected to be homogeneously covered in ligands, do not assemble into the typical spherical particle packing of face-centered cubic or body-centered cubic. Instead, they assemble into hexagonal arrangements typical for rods or wires.[41,57,58] Based on the sharpness of the peaks, the assemblies are expected to be highly ordered. Since particles remain un-sintered however, they are also sufficiently stabilized by alkylamine ligands. Similar hexagonal assemblies of ultrasmall nanoparticles, or clusters, have been described by Nevers *et al.* for CdS magic-sized clusters.[43] A possible explanation for this in the Sb_2S_3 system is that alkylamine ligands form a non-uniform coating despite lacking strong internal crystallinity. Since alkylamines are an L-type ligand with a demonstrated preference for cation-rich facets,[59,60] it is possible for Sb_2S_3 clusters to form a non-uniform coating on the particle. In this work however we do not experimentally confirm the coverage of ligands given the difficulty of this task due to the small size and low contrast of the particles."

To explore this possibility, syntheses in octylamine were performed with increasingly higher concentrations of another ligand, trioctylphosphine (TOP). The amount of nonpolar solvent, toluene, remained constant while octylamine was replaced with TOP. TOP was added to the reaction just before injecting the sulfur reagent, $(NH_4)_2S$. This prevented Sb^{3+} from being preferentially solvated by TOP, which might have slowed the kinetics of the reaction due to TOP's bulky alkyl tails. SAXS on samples with variable TOP concentrations from 0 to 10 wt% (Fig. 4A) show a continuously variable structure. As the TOP fraction increases, the 'rod-like' hexagonal assembly shifts to a face-centered cubic (FCC) spherical packing. The FCC phase is identified by reflections at ratios of $1q$, $\sqrt{4/3}q$, $\sqrt{8/3}q$, $\sqrt{11/3}q$, and $2q$ for the [111], [200], [220], and [222] directions respectively.[61,62] The gradual shift occurs with an increase of the [220] FCC peak, which becomes noticeable above 0.5 wt% TOP, as well as the splitting of the first peak into the [111] and [200] FCC reflections. A possible explanation for this behavior is that the trioctylphosphine is less nucleophilic than octylamine and therefore does not bind with as much site specificity. This would more fully coat the particle in ligands as more anion and cation sites would be

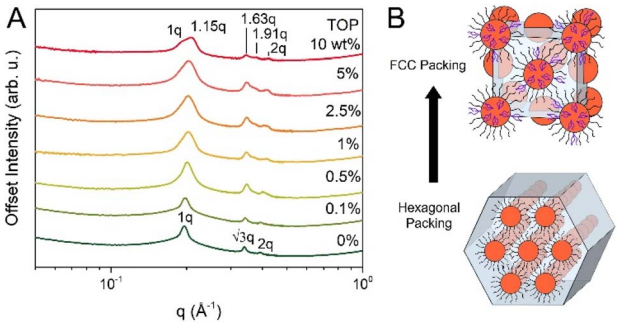

Fig. 4 (A) SAXS data of syntheses where octylamine was replaced with increasing amounts of TOP in solution which coincides with the structure transitioning from a hexagonal arrangement to an FCC structure. The FCC phase can be identified by the growth of the [220] peak (1.91q) and the splitting of the hexagonal structures' [100] peak into the [111] and [200] peak (1q and 1.15q respectively). (B) Graphic demonstrating the structure using only alkylamine ligand (black) and the increased axial spacing resulting in FCC packing using an addition of TOP (purple) to cover the surface.

passivated. As opposed to mostly cation sites when only octylamine is used. To confirm this mechanism in future studies, *ab initio* simulation and more thorough spectroscopy would be required to determine the exact binding site of the amine and phosphine ligands.

3.4. Electrochemical evaluation in battery electrodes

Since long alkyl groups are highly insulating,[63] it is necessary to remove them before preparing the Sb_2S_3 nanoparticles into electrodes. To do this, a ligand exchange procedure was followed using hydrazine, which has been shown to be an effective displacing agent for alkylamines on metal chalcogenides.[8,64] Nanoparticle samples were characterized in SAXS before (Fig. 5A) and after (Fig. 5B) the washing and ligand exchange procedure. After performing the ligand exchange, the assemblies of the nanoparticles were disrupted, and the particles deposited onto the glass vial. Once exchanged, the SAXS curve only features a single broad peak at 0.35 $Å^{-1}$ (1.8 nm), which is expected to represent the center-to-center distance between hydrazine coordinated nanoparticles of this size.

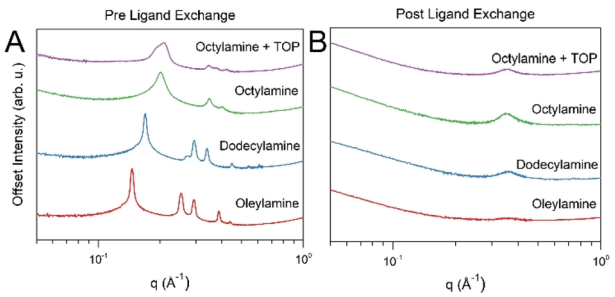

Fig. 5 SAXS spectra of (A) Sb_2S_3 particles before ligand exchange synthesized with oleylamine, dodecylamine, octylamine, as well as octylamine with 10 wt% trioctylphosphine (TOP). (B) After synthesizing, the particles were washed and ligand exchanged with hydrazine (procedure in methods) before being dispersed in water and characterized in SAXS. Both axes in log scale.

The electrochemical performance of ultrasmall Sb_2S_3 nanoparticles as negative electrodes for Li^+ and Na^+ ion batteries was evaluated. The data for Na^+ ion electrodes can be found in the SI (Fig. S16). To ensure consistency and reproducibility, the electrode slurry composition, slurry preparation, electrode fabrication, and testing environment using a coin cell configuration were standardized.

The only variable in these experiments was the choice of ligand (at 50 wt% in solution) during the nanoparticle synthesis prior to ligand exchange. For clarity, although the ligands are stripped, each sample is referred to by the ligand that was used during the sample's synthesis. In addition to SAXS, successful ligand exchanges were confirmed through Fourier-transformed infrared spectroscopy (FTIR) (Fig. S8). After ligand exchanging, the C–H bend peaks found between 3000 and 2850 cm^{-1} greatly decreased in intensity or disappeared in all samples regardless of choice of ligand.[65] The Sb_2S_3 nanoparticles can also be identified in the FTIR spectra. Characteristic Sb_2S_3 vibrational peaks at 721 cm^{-1} and 538 cm^{-1} are present,[66] as well as a peak characteristic of the metal–sulfide interaction at 1376 cm^{-1}.[67] Furthermore, the identity of the nanoparticles is confirmed with EDS (Fig. S9–S12) which demonstrates that before and after the ligand exchange the particles remain antimony(III) sulfide. These images also show that the aggregate size is not easily characterized in imaging techniques as the history of the sample's preparation plays a significant role in the size and morphology of secondary particle formation. Brunauer–Emmett–Teller (BET) analysis was used to characterize the surface area of nanoparticles synthesized with the four ligands (Table S1). The octylamine–TOP sample was measured to have the highest surface area at 33 $m^2\ g^{-1}$, followed by octylamine at 22 $m^2\ g^{-1}$, and then dodecylamine and oleylamine at 13 and 12 $m^2\ g^{-1}$ respectively.

Fig. 6A shows the redox peaks of ultrasmall Sb_2S_3 from lithiation and delithiation in the form of total differential capacity data. All samples exhibit distinct lithiation peaks between 1.2–1.5 V *vs.* Li^+/Li, corresponding to the solid electrolyte interphase (SEI) formation and the conversion reaction (eqn (1)). In the two electrodes prepared from nanoparticles synthesized in octylamine with 10 wt% TOP (Oct–TOP) as well as dodecylamine, a shoulder forms before the primary peak indicating intermediate reactions preceding the SEI formation. A second reduction peak at ~0.85 V represents the alloying reaction below (eqn (2)).[6–8,39] During delithiation, a broad oxidation peak near 1.0 V reflects the de-alloying of Li-ions from antimony. This is followed by a shallow peak between 1.5–2.0 V, attributed to the reverse conversion reaction.[8]

$$Sb_2S_3 + 6Li^+ + 6e^- \leftrightarrow 2Sb + 3Li_2S \quad (1)$$

$$2Sb + 6Li^+ + 6e^- \leftrightarrow 2Li_3Sb \quad (2)$$

Fig. 6B presents the charge–discharge profiles of the first cycle obtained at 0.3 A g^{-1}, a rate slow enough to capture

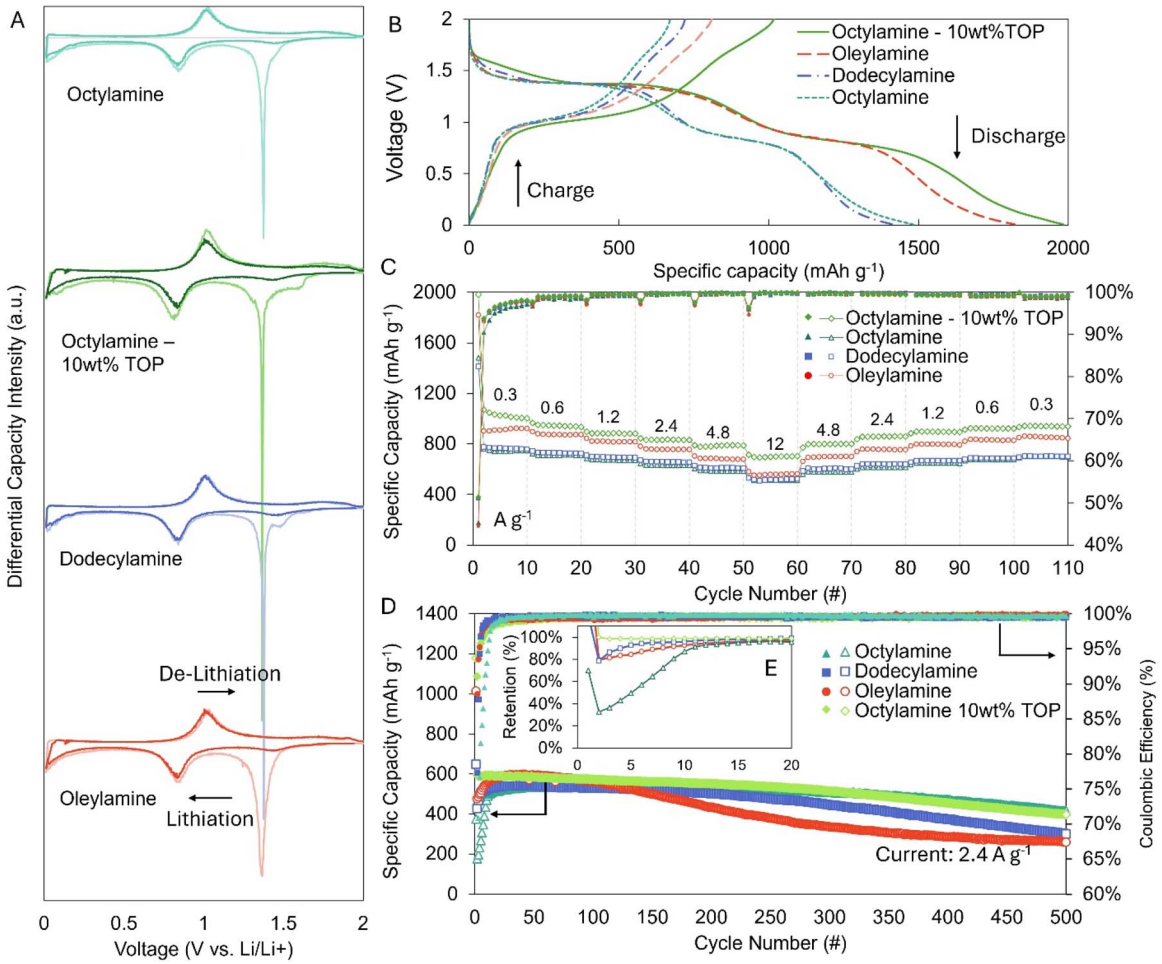

Fig. 6 Li-ion electrochemical data of the ultrasmall Sb_2S_3 synthesized in different ligating environments. (A) Total differential capacity data of the first (lighter) and second (darker) cycle for nanoparticles synthesized using identified alkylamine. (B) Galvanostatic charge–discharge curves of the first cycle. (C) Rate capacity. (D) Cycling stability data. (E) Normalized cycling stability data of the first 20 cycles.

detailed redox processes and the energy contributions of individual reactions. The lithiation profiles show distinct plateaus corresponding to the SEI formation, conversion, and alloying reactions, consistent with the total differential capacity peaks shown in Fig. 6A.[7] Notably, most of the irreversible capacity occurs above 1.2 V, which is evident from the difference in the total differential capacity data of the first and second cycle. As stated earlier, this region with the stark difference between the first and second cycle is primarily associated with SEI formation and initial conversion reactions.

Discharge capacities were highest for Oct–TOP at 1980 mAh g^{-1}, followed by oleylamine at 1816 mAh g^{-1}, octylamine alone at 1481 mAh g^{-1}, and dodecylamine at 1412 mAh g^{-1}. The subsequent charge capacities were approximately half of the first discharge capacities, consistent with irreversible SEI formation and side reactions in nanostructured materials, especially considering the high surface to volume ratio of these nanoparticles.

Other antimony sulfide nanocrystals in literature have exhibited an impressive specific capacity of 643 mAh g^{-1} (61% retention) when charged and discharged at a current of 12 A g^{-1}.[8] In our work, the ultrasmall Sb_2S_3 nanoparticles demonstrated similar rate capabilities, particularly for Oct–TOP, which had a capacity of ~700 mAh g^{-1} at 12 A g^{-1}, corresponding to 67% retention of its capacity measured at 0.3 A g^{-1}. Oleylamine had the next highest with 561 mAh g^{-1} (61% retention), while dodecylamine and octylamine exhibiting similar capacities with 510 and 521 mAh g^{-1}, respectively (67% retention for both). As shown in Fig. S13, with increasing current, less energy from the conversion reaction contributes to the overall capacity. This is due to the relatively large band gap (4.8 eV) of Li_2S, which is a major reason why lithium-sulfur batteries often have limited charging speed.[68–70] This also explains the 20% decrease in retention compared to that of antimony nanocrystals when fast charging/discharging.[38]

To assess the lifetime of the electrode, the electrodes were cycled at a relatively fast rate of 2.4 A g^{-1} until their capacity retention dropped to 50%. As shown in Fig. 6D, which shows the capacity data up to 500 cycles, the initial discharge capacities varied noticeably among the four electrode samples, reflecting differences in irreversible side reactions, including the SEI formation. The electrode prepared with Oct–TOP

demonstrated the highest initial capacity at 1177 mAh g^{-1}, followed by oleylamine (1014 mAh g^{-1}), dodecylamine (648 mAh g^{-1}), and octylamine (375 mAh g^{-1}).

As expected, capacity decreases over time, but their variations in the rate of decrease between samples is apparent. With Oct–TOP reaching 67% retention at 500th cycle (80% at 370th cycle). Similarly, both octylamine and dodecylamine exhibited a gradual capacity decrease. Once the capacity reached 597 mAh g^{-1} for octylamine, it slowly degraded, whereby at 500th cycle showed 77% retention (80% at 480th cycle). With dodecylamine, once the capacity reached 541 mAh g^{-1}, the capacity decreased to 55% retention (80% at 318th cycle). As for oleylamine, similar to the cycle life data shown with previously showcased Sb_2S_3 nanoparticles prepared using oleylamine as the coordinating ligand, the capacity degraded until 380th cycle upon which it plateaued around 50% capacity retention (80% at 167th cycle).[8]

Performing electrochemical impedance spectroscopy (EIS) before and after the first 20 cycles corroborates this (Fig. 7). The nanoparticles synthesized with octylamine with TOP showed the smallest change in resistive impedance (Z') and capacitive impedance ($-Z''$) response pre and post cycling at 2.4 A g^{-1}, which demonstrates its stability and lack of rearrangement during activation cycling. This suggests that the electrode composite has a more favorable structure when synthesized using octylamine with TOP compared to the other samples. By comparison, oleylamine's charge transfer resistance increased significantly after the 20 cycles, while octylamine and dodecylamine both decreased suggesting their arrangement was less optimal pre activation cycling. This rearrangement during initial cycling is a common phenomenon.[71–73] EIS also provides further insight into the performance of the Oct–TOP samples compared to the other synthesized materials. The smaller real and imaginary impedance in the higher frequency region (left side of Nyquist plot) of the Oct–TOP sample as well as the steeper rise in imaginary impedance at low frequencies (right side of Nyquist plot, Warburg region) indicate that the impedance is dominated by capacitative limitation rather than diffusive limitation. Whereas, with the Oct sample, the onset of diffusion-controlled behavior or the transition point to the Warburg region is preceded by the heavily diffusion limited plateau that is parallel to the real axis. This is a behavior that's observed in systems that have a significant particle depth causing limited long-range ion penetration caused by a variety of possible factors including low effective surface area, finite-length diffusion, or interfacial polarization.[74]

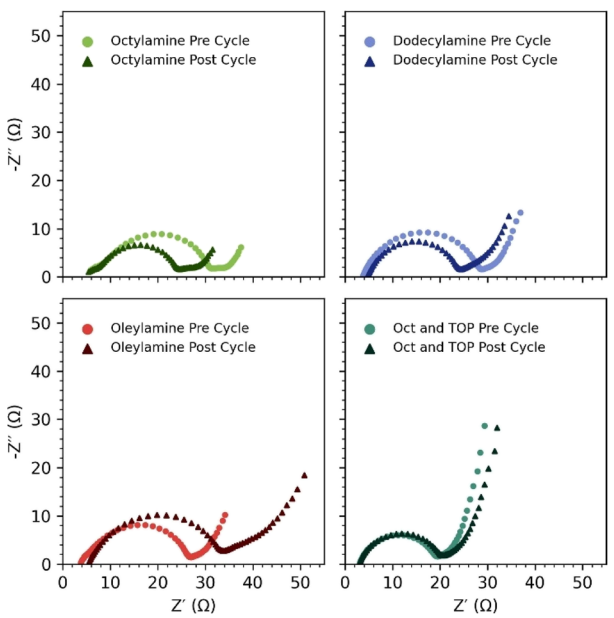

Fig. 7 Electrochemical impedance spectra of electrodes prepared with Sb_2S_3 nanoparticles synthesized using octylamine (oct), dodecylamine, oleylamine, and octylamine with trioctylphosphine (TOP) before and after cycling 20 times at 2.4 A g^{-1}.

Altogether, this work shows that the ultrasmall Sb_2S_3 nanoparticles performed the best when synthesized in a solution of 50 wt% toluene, 40 wt% octylamine, and 10 wt% trioctylphosphine (Oct–TOP). Over 500 cycles at 2.4 A g^{-1}, Oct–TOP experienced a similar drop in specific capacity to octylamine, but exhibited excellent rate capability, outperforming all other samples. When adding TOP, the SEI layer formation appears to be impacted as is evidenced by the slight difference in shape of the galvanostatic lithiation/delithiation curves between the Oct–TOP and octylamine samples as seen in Fig. 6B. Providing more evidence of its improved electrochemical performance, higher lithiation percentages in the alloying and conversion reactions were measured for the Oct–TOP sample as shown in Fig. S14. Additionally, the Oct–TOP sample required fewer initial cycles to reach its maximum capacity. All other samples exhibited a gradual capacity increase during the initial cycles as can be seen in the inset of Fig. 6D. Eventually, each stabilized at 537 mAh g^{-1} for octylamine, 541 mAh g^{-1} for dodecylamine, and 597 mAh g^{-1} for oleylamine. In addition, to investigate the cause of performance differences, we conducted differential capacity analysis over the first 100 cycles (Fig. S15A–D), as well as from 100 to 50% capacity retention (Fig. S15E–H). The data reveal distinct changes in redox peak shape and position, particularly during activation, where redox features become more defined. Samples prepared with octylamine and dodecylamine exhibit broader and more polarized redox peaks, indicative of sluggish kinetics and higher internal resistance. In contrast, samples synthesized with TOP and oleylamine exhibit narrower peaks and lower polarization, correlating with improved electrochemical performance. Differential capacity analysis also sheds light on degradation pathways, especially noted in Fig. S15E–H. All samples show unique peak formations and fading, which suggest that ligand identity, and by extension particle aggregation and size or some other factors, plays a significant role in electrochemical behavior. This suggests the importance of the synthesis procedure and packing behavior regardless of whether the initial ligating environment has been removed. The synthesis path or mechanism could be important factors to consider especially for particles in this size regime that self-assemble.

4. Discussion

Assembly is a commonality between many systems with ultrasmall building blocks.[26,48,75] It is often attributed to strong registry along preferred crystallographic directions, which can be followed by sintering.[27,32,76,77] In this work, the Sb_2S_3 particles lack strong atomic lattice spacings and remain unsintered (Fig. S2 and S3). This indicates that the particles are aligning *via* well-coordinated ligands. While the length of the ligands affects the distance between the particles, the concentration of ligands in solution also affects the spacing to a lesser extent. As the concentration of ligands increases, the interparticle spacing decreases (Fig. 2). At lower ligand concentrations, when the solution is mostly toluene, the ligands on the surface extend since nonpolar toluene is a 'good solvent' for nonpolar alkyl groups. When the solution has a much higher concentration of ligand, the ligand contracts on average since the nonpolar alkyl group is not as strongly solvated.[30,78] This effect also explains the narrowing of the peaks in the octylamine series (Fig. 2A) where the structure of the assembly becomes more homogeneous as the ligands contract and spacing decreases.

In all Sb_2S_3 nanoparticles synthesized with alkylamines, the packing was 'rod-like' and hexagonal (Fig. 2). Only when trioctylphosphine (TOP) was added did the packing change to a close packed face-centered cubic arrangement (Fig. 4). We postulate that this is due to the primary particles being more fully covered by ligands given that trioctylphosphine would bind with less site-specificity.[59,60] In addition, it has been shown that trioctylphosphine readily oxidizes to form trioctylphosphine oxide when used in open-to-air reactions.[79] Trioctylphosphine oxide coordinates preferentially into cation vacancies as an electron acceptor,[80] making it more likely to fully cover the Sb_2S_3 particles in conjunction with alkylamines, electron donating L-type ligands. In control experiments, the addition of 10 wt% trioctylphosphine oxide also resulted in the FCC structure (Fig. S7).

The effect that different alkyl phosphine or amine ligands might have on a ligand exchange is rarely discussed in literature as it relates to ultrasmall particles or electrochemical applications. In this work, the length of the alkylamine ligand is inversely proportional to the overall performance of the battery, where smaller ligands improve cycling and specific capacities even after a complete ligand exchange was performed. The addition of trioctylphosphine was also found to improve specific capacity and reduce or eliminate the number of cycles needed to reach a more stable capacity. The phenomenon of increasing capacity over the first few initial cycles is commonly referred to as activation cycling. It is attributed to the gradual rearrangement of the active material, conductive medium, and binder into a more kinetically favorable configuration.[71–73] Activation cycling is often more pronounced in systems where nanoparticles are highly bridged or aggregated into secondary particles.[71] Since the trioctylphosphine containing sample requires fewer, or no, activation cycles, it suggests that the particles are in a more favorable arrangement before cycling. In a half-cell configuration with a plentiful lithium reserve from a lithium metal counter electrode, this behavior may seem minor. However, in a full-cell configuration with balanced capacities in the negative and positive electrodes, capacity may fade due to repeated exposure of active materials to the electrolyte, reducing the benefits of high energy density materials. Even if the positive electrode mass is increased or an active material like lithium iron oxide (Li_2FeO_3) is used to compensate for SEI layer growth, the overall battery capacity would still be limited.

We postulate that the variances in the battery data, including differences in capacity degradation behavior observed in the differential capacity analysis shown in Fig. S14, may result from size and morphology differences in the aggregated particles after ligand exchange. The higher surface area of the Oct–TOP sample measured with BET (Table S1) would support a difference in secondary particle morphology resulting in a higher surface area which may be an explanation for its difference in electrochemical performance compared to the other samples. Unfortunately, the ligand exchange strategy used in numerous past studies,[8,21,38,64,81] typically involving redispersing the material in a solvent of opposite polarity with a chosen ligand, lacks the necessary details to definitively determine the cause. Post-analysis often only highlights differences in chemical structure before and after ligand exchange using techniques such as attenuated total reflectance Fourier transform infrared (ATR-FTIR) spectroscopy.[2,8,38,65,81] This work also demonstrates that the majority of the alkyl chains were effectively removed (Fig. S8). Nonetheless, the battery data reveals differences in electrochemical performance in various aspects. We believe the variations in secondary particles stem from factors during and after the synthesis such as the assembly and packing density of the nanoparticles before and during the ligand exchange.

5. Conclusion

The synthesis of ultrasmall antimony(III) sulfide (Sb_2S_3) particles is reported using a room temperature, open-air procedure. Self-assembly of ultrasmall nanoparticles is characterized *via* small angle X-ray scattering, showing the formation of elongated hexagonal structures typically found in rod-like particles and micelles. This assembly is modified by adjusting the ligands and/or the solvent, with longer ligands, as well as lower concentrations of ligand in solution, increasing the interparticle spacing. The unusual hexagonal structure is proposed to be caused by a non-uniform coordination of alkylamines over the Sb_2S_3 surface. Using an additional ligand (trioctylphosphine), which lacks in binding selectivity, leads to the formation of an FCC phase. The performance of Sb_2S_3 nanoparticles in Li^+ battery electrodes is exceptional, demonstrating over 500 cycles above 80% retention, as well as cycling up to 12C with a relatively small drop in capacity. The ligand used in the nanoparticle synthesis is also shown to impact the performance of electrodes even after a ligand exchange. This suggests that ligand identity is an important design criterion that cannot be overlooked regardless of how similar the final nanoparticle morphology may appear.

Author contributions

ZRW, GKL, SL, VCH, LDP conceptualization; ZRW and GKL – performed synthesis and ligand exchange; ZRW, GKL, LDP – data analysis, manuscript writing and editing; ZRW and GKL – figure preparation; ZRW, AM, LDP – conducted and analyzed SAXS; GR and JCI – conducted TEM; GKL and SL – conducted and analyzed XRD; ZRW – conducted and analyzed FTIR; GKL and PJP – performed electrode and battery assembly, conducted electrochemical characterization (battery testing and EIS), conducted BET.

Conflicts of interest

The authors declare there are no conflicts of interest that would influence the findings within this work.

Data availability

The data supporting this article have been made available within the article and SI.

Provided in the supplementary information are high angle annular dark field scanning transmission electron images, small angle X-ray scattering data, X-ray diffraction data, attenuated transmission reflectance Fourier transformed infrared spectra, results of Brunauer–Emmett–Teller analysis, scanning electron microscopy images, electrochemical characterization for anodes made from Sb_2S_3 nanoparticles including charge and discharge curves, normalized galvanostatic lithiation and delithiation curves, total differential capacity data, and rate capacity for sodium ion system. See DOI: **https://doi.org/10.1039/d5ta04184h**.

Acknowledgements

This work was primarily supported by the National Science Foundation (NSF) through the University of Washington Molecular Engineering Materials Center, a Materials Research Science and Engineering Center (DMR-2308979). The authors also acknowledge the use of facilities and instrumentation supported by the U.S. National Science Foundation through the Major Research Instrumentation (MRI) program (DMR-2116265) as well as the University of Washington Molecular Analysis Facility, which is supported in part by funds from the Molecular Engineering & Sciences Institute, the Clean Energy Institute, and the National Science Foundation (NNCI-2025489 and NNCI-1542101).

References

1 R. Gusmão, Z. Sofer, J. Luxa and M. Pumera, *ACS Sustainable Chem. Eng.*, 2019, **7**, 15790–15798.
2 P. A. Chate, S. D. Lakde and D. J. Sathe, *Optik*, 2022, **250**, 168296.
3 R. Kondrotas, C. Chen and J. Tang, *Joule*, 2018, **2**, 857–878.
4 S.-J. Moon, Y. Itzhaik, J.-H. Yum, S. M. Zakeeruddin, G. Hodes and M. Grätzel, *J. Phys. Chem. Lett.*, 2010, **1**, 1524–1527.
5 X. Huang, H. Woo, P. Wu, Q. Wang, G. Tan and J. W. Choi, *J. Alloys Compd.*, 2019, **777**, 866–871.
6 Z. Yuan, Z. Zeng, W. Zhao, Y. Dong, H. Lei, B. Wang, Y. Yang, W. Sun and P. Ge, *ACS Appl. Energy Mater.*, 2023, **6**, 12139–12165.
7 D. Y. W. Yu, H. E. Hoster and S. K. Batabyal, *Sci. Rep.*, 2015, **4**, 4562.
8 K. V. Kravchyk, M. V. Kovalenko and M. I. Bodnarchuk, *Sci. Rep.*, 2020, **10**, 2554.
9 P. Bayliss and W. Nowacki, *Z. Kristallogr. Cryst. Mater.*, 1972, **135**, 308–315.
10 M. Y. Versavel and J. A. Haber, *Thin Solid Films*, 2007, **515**, 7171–7176.
11 M. A. Grasser, T. Pietsch, E. Brunner and M. Ruck, *Dalton Trans.*, 2022, **51**, 4079–4086.
12 R.-D. Sun and T. Tsuji, *Appl. Surf. Sci.*, 2015, **348**, 38–44.
13 D. V. Talapin, J.-S. Lee, M. V. Kovalenko and E. V. Shevchenko, *Chem. Rev.*, 2010, **110**, 389–458.
14 Y. Jing, X. Liu, Y. Xu, M. Zhang, R. Li, S. Wang, Z. Yan, W. Sun, J. Wu and Z. Lan, *Chem. Eng. J.*, 2023, **455**, 140871.
15 J. Zhu, X. Yan and J. Cheng, *Nanoscale Res. Lett.*, 2018, **13**, 19.
16 J. H. Zhang, Z. Chen, Z. L. Wang and N. B. Ming, *J. Mater. Res.*, 2003, **18**, 1804–1808.
17 M. Abulikemu, S. Del Gobbo, D. H. Anjum, M. A. Malik and O. M. Bakr, *J. Mater. Chem. A*, 2016, **4**, 6809–6814.
18 R. Malakooti, L. Cademartiri, A. Migliori and G. A. Ozin, *J. Mater. Chem.*, 2008, **18**, 66–69.
19 M. Pal, N. R. Mathews and X. Mathew, *J. Mater. Res.*, 2017, **32**, 530–538.
20 J. Chao, B. Liang, X. Hou, Z. Liu, Z. Xie, B. Liu, W. Song, G. Chen, D. Chen and G. Shen, *Opt. Express*, 2013, **21**, 13639.
21 V. Lojpur, M. Joschko, C. Graf, N. Radmilović, M. Novaković and I. Validžić, *Mater. Sci. Semicond. Process.*, 2022, **137**, 106196.
22 S. M. Hwang, J. Kim, Y. Kim and Y. Kim, *J. Mater. Chem. A*, 2016, **4**, 17946–17951.
23 B. F. Variano, D. M. Hwang, C. J. Sandroff, P. Wiltzius, T. W. Jing and N. P. Ong, *J. Phys. Chem.*, 1987, **91**, 6455–6458.
24 B. M. Cossairt and J. S. Owen, *Chem. Mater.*, 2011, **23**, 3114–3119.
25 M. Hu, J. Liu, W. Guo, X. Liu, G.-M. Rignanese and T. Yang, *Chem. Mater.*, 2024, **36**, 7108–7116.
26 S. Busatto and C. De Mello Donega, *ACS Mater. Au*, 2022, **2**, 237–249.
27 S. Wan, X. Xi, H. Zhang, J. Ning, Z. Zheng, Z. Zhang, Y. Long, Y. Deng, P. Fan, D. Yang, T. Li and A. Dong, *ACS Nano*, 2022, **16**, 21315–21323.
28 N. Ostrovsky, G. Le Saux, U. Argaman, I. Chen, T. Chen, C.-H. Chang, G. Makov and M. Schvartzman, *Langmuir*, 2021, **37**, 9098–9110.
29 Y. Zhou, X. Ma, L. Zhang and J. Lin, *Phys. Chem. Chem. Phys.*, 2017, **19**, 18757–18766.
30 R. M. Choueiri, E. Galati, H. Thérien-Aubin, A. Klinkova, E. M. Larin, A. Querejeta-Fernández, L. Han, H. L. Xin,

O. Gang, E. B. Zhulina, M. Rubinstein and E. Kumacheva, *Nature*, 2016, **538**, 79–83.
31 H. Wang, H. Li, P. Gu, C. Huang, S. Chen, C. Hu, E. Lee, J. Xu and J. Zhu, *Nanoscale*, 2023, **15**, 2018–2035.
32 W. Lv, W. He, X. Wang, Y. Niu, H. Cao, J. H. Dickerson and Z. Wang, *Nanoscale*, 2014, **6**, 2531–2547.
33 B. Gao, G. Arya and A. R. Tao, *Nat. Nanotechnol.*, 2012, **7**, 433–437.
34 A. Loubat, M. Impéror-Clerc, B. Pansu, F. Meneau, B. Raquet, G. Viau and L.-M. Lacroix, *Langmuir*, 2014, **30**, 4005–4012.
35 S. Bettscheider, T. Kraus and N. A. Fleck, *Acta Mater.*, 2022, **231**, 117799.
36 S. I. Stoeva, B. L. V. Prasad, S. Uma, P. K. Stoimenov, V. Zaikovski, C. M. Sorensen and K. J. Klabunde, *J. Phys. Chem. B*, 2003, **107**, 7441–7448.
37 K. Bian, H. Schunk, D. Ye, A. Hwang, T. S. Luk, R. Li, Z. Wang and H. Fan, *Nat. Commun.*, 2018, **9**, 2365.
38 M. He, K. Kravchyk, M. Walter and M. V. Kovalenko, *Nano Lett.*, 2014, **14**, 1255–1262.
39 Z. Li, H. Du, J. Lu, L. Wu, L. He and H. Liu, *Chem. Phys. Lett.*, 2021, **771**, 138529.
40 H. Zhang, B.-R. Hyun, F. W. Wise and R. D. Robinson, *Nano Lett.*, 2012, **12**, 5856–5860.
41 T. Hashimoto, T. Kawamura, M. Harada and H. Tanaka, *Macromolecules*, 1994, **27**, 3063–3072.
42 N.-W. Hsu, B. Nouri, L.-T. Chen and H.-L. Chen, *Macromolecules*, 2020, **53**, 9665–9675.
43 D. R. Nevers, C. B. Williamson, B. H. Savitzky, I. Hadar, U. Banin, L. F. Kourkoutis, T. Hanrath and R. D. Robinson, *J. Am. Chem. Soc.*, 2018, **140**, 3652–3662.
44 N. Geva, J. J. Shepherd, L. Nienhaus, M. G. Bawendi and T. Van Voorhis, *J. Phys. Chem. C*, 2018, **122**, 26267–26274.
45 J. Borges, J. A. Ribeiro, E. M. Pereira, C. A. Carreira, C. M. Pereira and F. Silva, *J. Colloid Interface Sci.*, 2011, **358**, 626–634.
46 M. Grzelczak, J. Vermant, E. M. Furst and L. M. Liz-Marzán, *ACS Nano*, 2010, **4**, 3591–3605.
47 C. Yi, Y. Yang, B. Liu, J. He and Z. Nie, *Chem. Soc. Rev.*, 2020, **49**, 465–508.
48 K. Yu, *Adv. Mater.*, 2012, **24**, 1123–1132.
49 S. M. Harrell, J. R. McBride and S. J. Rosenthal, *Chem. Mater.*, 2013, **25**, 1199–1210.
50 B. Michen, C. Geers, D. Vanhecke, C. Endes, B. Rothen-Rutishauser, S. Balog and A. Petri-Fink, *Sci. Rep.*, 2015, **5**, 9793.
51 N. J. Fernandes, H. Koerner, E. P. Giannelis and R. A. Vaia, *MRS Commun.*, 2013, **3**, 13–29.
52 E. Rabani, D. R. Reichman, P. L. Geissler and L. E. Brus, *Nature*, 2003, **426**, 271–274.
53 Z. Cui, K. Bu, Y. Zhuang, M.-E. Donnelly, D. Zhang, P. Dalladay-Simpson, R. T. Howie, J. Zhang, X. Lü and Q. Hu, *Commun. Chem.*, 2021, **4**, 125.
54 C. J. Gommes, S. Jaksch and H. Frielinghaus, *J. Appl. Crystallogr.*, 2021, **54**, 1832–1843.
55 A. L. Patterson, *Phys. Rev.*, 1939, **56**, 978–982.
56 N. Ikawa, Y. Oumi, T. Kimura, T. Ikeda and T. Sano, *J. Mater. Sci.*, 2008, **43**, 4198–4207.
57 S. C. McGuire, Y. Zhang and S. S. Wong, *Nanotechnology*, 2022, **33**, 475602.
58 L. Vigderman, B. P. Khanal and E. R. Zubarev, *Adv. Mater.*, 2012, **24**, 4811–4841.
59 N. G. Mbewana-Ntshanka, M. J. Moloto and P. K. Mubiayi, *Heliyon*, 2020, **6**, e05130.
60 S. Mourdikoudis, M. Menelaou, N. Fiuza-Maneiro, G. Zheng, S. Wei, J. Pérez-Juste, L. Polavarapu and Z. Sofer, *Nanoscale Horiz.*, 2022, **7**, 941–1015.
61 H. Matsuoka, H. Tanaka, T. Hashimoto and N. Ise, *Phys. Rev. B:Condens. Matter Mater. Phys.*, 1987, **36**, 1754–1765.
62 L.-T. Chen, C.-Y. Chen and H.-L. Chen, *Polymer*, 2019, **169**, 131–137.
63 Y. Liu, M. Gibbs, J. Puthussery, S. Gaik, R. Ihly, H. W. Hillhouse and M. Law, *Nano Lett.*, 2010, **10**, 1960–1969.
64 D. V. Talapin and C. B. Murray, *Science*, 2005, **310**, 86–89.
65 M. Liu, Y.-Y. Wang, Y. Liu and F.-L. Jiang, *J. Phys. Chem. C*, 2020, **124**, 4613–4625.
66 L. Dashairya, M. Sharma, S. Basu and P. Saha, *J. Alloys Compd.*, 2018, **735**, 234–245.
67 S. Subramanian, P. Chithra Lekha and D. Pathinettam Padiyan, *Phys. B*, 2010, **405**, 925–931.
68 M. Zhao, H.-J. Peng, B.-Q. Li and J.-Q. Huang, *Acc. Chem. Res.*, 2024, **57**(4), 545–557.
69 S. Chakrabarti, A. Singh and A. K. Thakur, *J. Electrochem. Soc.*, 2024, **171**, 030525.
70 R. S. Assary, L. A. Curtiss and J. S. Moore, *J. Phys. Chem. C*, 2014, **118**, 11545–11558.
71 M. F. Oszajca, M. I. Bodnarchuk and M. V. Kovalenko, *Chem. Mater.*, 2014, **26**, 5422–5432.
72 J. Casella, J. Morzy, E. Gilshtein, M. Yarema, M. H. Futscher and Y. E. Romanyuk, *ACS Nano*, 2024, **18**, 4352–4359.
73 M. M. S. Sanad and A. Toghan, *Surf. Interfaces*, 2021, **27**, 101550.
74 A. Ch. Lazanas and M. I. Prodromidis, *ACS Meas. Sci. Au*, 2023, **3**, 162–193.
75 Z. Tang, Z. Zhang, Y. Wang, S. C. Glotzer and N. A. Kotov, *Science*, 2006, **314**, 274–278.
76 C. J. Dalmaschio, C. Ribeiro and E. R. Leite, *Nanoscale*, 2010, **2**, 2336.
77 J. H. Yu, J. Joo, H. M. Park, S.-I. Baik, Y. W. Kim, S. C. Kim and T. Hyeon, *J. Am. Chem. Soc.*, 2005, **127**, 5662–5670.
78 E. Galati, H. Tao, C. Rossner, E. B. Zhulina and E. Kumacheva, *ACS Nano*, 2020, **14**, 4577–4584.
79 W. Wang, S. Banerjee, S. Jia, M. L. Steigerwald and I. P. Herman, *Chem. Mater.*, 2007, **19**, 2573–2580.
80 G. K. Grandhi, M. Arunkumar and R. Viswanatha, *J. Phys. Chem. C*, 2016, **120**, 19785–19795.
81 K. V. Kravchyk, L. Piveteau, R. Caputo, M. He, N. P. Stadie, M. I. Bodnarchuk, R. T. Lechner and M. V. Kovalenko, *ACS Nano*, 2018, **12**, 8297–8307.